CCFE
CULHAM CENTRE FOR FUSION ENERGY

UK Atomic Energy Authority

UKAEA-CCFE-PR(23)122

Bin Zhu, Nathanael Leung, Yiqiang Wang, Hannah, Zhang, Jiří Dluhoš, Thilo Pirling, Michael Gorley, Mark J. Whiting, Tan Sui

Investigation of the residual strain and deformation mechanisms in laser-welded Eurofer97 steel for fusion reactors

Investigation of the residual strain and deformation mechanisms in laser-welded Eurofer97 steel for fusion reactors

Bin Zhu, Nathanael Leung, Yiqiang Wang, Hannah, Zhang, Jiří Dluhoš, Thilo Pirling, Michael Gorley, Mark J. Whiting, Tan Sui

This is a preprint of a paper submitted for publication in
Journal of Advanced Research

Investigation of the residual strain and deformation mechanisms in laser-welded Eurofer97 steel for fusion reactors

Bin Zhu[1], Nathanael Leung[1], Yiqiang Wang[2], Hannah, Zhang[3], Jiří Dluhoš[4], Thilo Pirling[5], Michael Gorley[2], Mark J. Whiting[1], Tan Sui[1,3]*

[1] School of Mechanical Engineering Sciences, University of Surrey, Guildford, Surrey, GU2 7XH, UK

[2] United Kingdom Atomic Energy Authority, Culham Centre for Fusion Energy, Culham Science Centre, Abingdon, Oxon, OX14 3DB, UK

[3] National Physical Laboratory, Hampton Road, Teddington TW11 0LW, UK

[4] TESCAN ORSAY HOLDING, a.s., Libušina třída 21, 623 00 Brno, Czech Republic

[5] Diffraction, Institut Max von Laue – Paul Langevin (ILL), 71, avenue des Martyrs – CS 20156, Grenoble cedex 9, 38042 France

* Corresponding author: t.sui@surrey.ac.uk;

Abstract

A fusion power plant requires not only the control of the high energy plasma but also advanced techniques for maintenance and assembly in order to generate electricity consistently and safely. Laser welding is a promising technique for cutting and joining pipes and in-vessel components made of Eurofer97, a European baseline structural material. However, the substantial residual strain, usually induced during post weld cooling, degrades the mechanical properties and reduces the lifespan of engineering components. Establishing the underpinning mechanistic connection between residual strain, microstructural change, and tensile behaviour is a critical aspect of the lifetime assessment of critical engineering components. Here, the heterogeneous strain evolution in laser-welded Eurofer97 joint is quantitatively evaluated using *in situ* neutron diffraction at the lattice scale, nanoindentation at the microscale and digital image correlation (DIC) at a macroscale. The residual lattice strain in the loading direction is characterised via neutron diffraction and validated using a plasma-focused ion beam (PFIB-DIC) ring-core method. Superimposing the microstructural strengthening, the highest residual tensile strain ($-1 \times 10^{-3}\mu\varepsilon$) accelerates the accumulation of tensile deformation around the fusion line (FZ/HAZ interface), whereas residual compressive strain ($0.6 \times 10^{-3}\mu\varepsilon$) hinders the tensile strain evolution around the heat-affected zone and the base material interfaces, increasing the localised yield strength to 506 MPa. Residual strain is the primary strengthening mechanism during the initial deformation stage, although the microstructural strengthening then dominates as deformation increases. This work reveals the critical role of residual strain and microstructural effects on tensile behaviour, and the results provide insight into managing structural integrity and developing predictive tools for lifetime assessment.

1. Introduction

Residual strain is one of the vital assessment factors of structural integrity. It is the locked-in strain induced by welding processes after the removal of all external loads. It is well-known that residual strain associated with complex microstructures notably affects the mechanical properties [1–6]. Residual strain is highly detrimental, as it can be responsible for various engineering problems such as distortion, stress corrosion cracking, fatigue, and degradation of tensile strength [7]. To address the deleterious residual strain related effects, and ensure safety and longevity, it is crucial to establish a fundamental understanding of the deformation mechanism associated with residual strain. This is especially challenging in complex materials systems, such as those in the nuclear power industry.

Nuclear fusion is a potential source of green power that could end humanity's reliance on fossil fuels and the well-known environmentally damaging carbon emissions that come with them. In the quest for this new source of energy, a series of fusion tokamaks have been or are being investigated, from the Joint European Torus (JET) and the International Thermonuclear Experimental Reactor (ITER), to the DEMOnstration power plant (DEMO) [8]. To meet the demands of low radiation activities, high-temperature mechanical performance, and appropriate thermal conductivity, the reduced-activation ferritic/martensitic (RAFM) steels were developed. They are based on high Cr Grade 91 steel by replacing Mo and Nb with lower activation elements like W and Ta [4,9–11]. One such RAFM is Eurofer97 which is currently the European baseline structural material for the pipe and in-vessel components (e.g., breeding blanket and divertor cassette) for the EU-DEMO [12–14]. The assembly and maintenance of these in-vessel components presents difficulties because of the internal grid structures [5]. Rapid reliable welding and joining techniques are required to maintain the structural integrity of these breeding blanket joints.

Laser welding is considered one of the most promising techniques because its equipment is compact and portable, and it enables full penetration of single-pass welds in thick sections. The low heat input of laser welding process leads to a narrow weld and heat-affected zone. Combining laser welding with a robotic device could enable cutting and welding operations in complex working conditions [3]. Previous studies have demonstrated the feasibility of remote laser tools to manufacture and maintain the in-vessel components in fusion plants by laser welding [3,6,15]. However, the non-uniform thermal expansion and phase transformations give a rise to residual strain and local distortion [16–18]. Such residual strain can negatively affect mechanical properties, such as yield strength, fracture toughness and ultimate tensile strength (UTS), which are indispensable for the design protocol of nuclear fusion components. Heterogeneous residual strain over the sub-regions of the weldment in association with microstructures aggravate crack initiation and propagation at the interface of two sub-regions.

Efforts have been made to quantify multi-scale residual stress and strain experimentally in laser-welded Eurofer97 joints using neutron diffraction, neutron Bragg edge imaging, plasma focused ion beam, digital image correlation (PFIB-DIC) and nanoindentation, and predictions of residual stress and strain have been achieved via a finite element analysis (FEA) simulation [19–21]. Whilst previous studies established the interactions of residual strain with microstructure substantial changes in micro-hardness [20], establishing micro-hardness alone is insufficient for a comprehensive analysis of residual strain effects. The tensile behaviour is usually required to demonstrate the yield strength for lifetime assessments of engineering components. Investigations on the tensile deformation mechanism have only been achieved with correlation to microstructures in a Eurofer97 joint. For example, the strain evolution of laser-welding Eurofer97 was characterised using a DIC technique and compared with that of the post-welded heat treatment (PWHT), where the microstructure is restored [22]. Nevertheless, exactly how the residual strain distributes in the loading direction, and its effect on the tensile deformation remains unclear. This incomplete understanding prevents a full appreciation of the underpinning deformation mechanisms operating in laser-welded Eurofer97 steel.

Here, the deformation mechanism of the laser-welded Eurofer97 joint is studied experimentally by comparing the tensile strain evolution in an as-welded joint with a PWHT joint, measured by *in situ* neutron diffraction and a DIC technique. Prior to loading, neutron diffraction was applied to quantify the residual strain distribution across the weldment, and the microstructural distribution was investigated using electron backscatter diffraction (EBSD). As the diffraction technique is vulnerable to microscale residual strain and compositions, the PFIB-DIC was used to validate that the lattice residual strain is representative of the macroscale residual strain. By studying the tensile behaviour in the fusion zone (FZ), heat-affected zone (HAZ), and base material (BM) regions, the interactions with residual strain and microstructures were explored. This investigation establishes an underpinning understanding of the deformation mechanism, which provide insight into optimising the remote welding processes for the fusion power plant components so as to improve the longevity of the fusion reactor.

2. Materials and Methods

2.1. Materials and microstructural characterisation

Eurofer97 steel made by Böhler Austria GmbH, with a composition of Fe-0.11C-8.82Cr-1.08W-0.13Ta-0.48Mn-0.20 V (in wt.%), was used in the present investigation. The detailed fabrication, rolling processes, and heat treatment of Eurofer97 steel were described in a previous study [23]. The

parameters used for the laser-welding and PWHT were presented previously [21]. For the tensile tests, flat dog-bone specimens were designed based on the ASTM E8 standard size with a gauge length of 25 mm and a cross-section of 6 × 6 mm^2 and cut from the laser-welded Eurofer97 plate using electrical discharge machining. To provide a stress-free (d_0) reference for neutron diffraction analysis, as-welded sample and PWHT samples were cut into a comb-shape to release the residual strain in the loading direction. The microstructure was characterised along the centre line of the laser-welded Eurofer97 joint using EBSD, as shown in **Fig. 1**(a). The EBSD maps were recorded using a Joel-7100F with an accelerating voltage of 20 kV equipped with a Thermo Fisher Lumis EBSD detector using a step size of 500 nm. The post-data treatment was achieved using the MTEX 5.2.8 MATLAB toolbox [24], and the average grain size in the FZ, HAZ, and BM regions was measured from the EBSD orientation maps using the mean linear intercept method [25].

2.2. Lattice residual strain and lattice strain evolution characterised using neutron diffraction

The strain characterisation was performed using the SALSA monochromatic neutron diffraction instrument at the Institut Laue-Langevin, France, with a gauge volume of 0.6 × 0.6 × 2 mm^3 to obtain high-resolution strain data in the sub-regions of the weldment (**Fig. 1**(a)). The grain family whose crystal plane is normal to *<110>* lies along the loading direction is designated as *<110>//LD*. A wavelength of 1.685 Å was used to measure the *<110>//LD* grain family in the loading direction. Prior to the tensile loading, neutron diffraction measurements were performed to measure the residual strain distribution. This was achieved by taking line-scan measurements across the weldment at 0.3 mm intervals, characterising the material at five different depths (from 1 mm to 5 mm below the top surface). The uniaxial tensile load was then applied in a step-load controlled manner where the maximum loading stress applied (610 MPa) was below the ultimate tensile stress (UTS). At each load step of the loading and unloading procedure *in situ* neutron diffraction measurements were carried out by performing a line scan across the weldment at the mid-thickness position, as illustrated in the inset figure in **Fig. 1**(a). To ensure the quality of the diffraction patterns, 1500 neutron statistics were acquired at each datapoint. The diffraction spectra were then analysed to obtain scattering angle, *2θ*, for lattice strain calculation and the full width at half maximum (FWHM) for microstructure analysis [26].

2.3. Macroscopic strain evolution using DIC

The lab-based uniaxial tension experiments were carried out using the same geometry dog-bone samples, and the tensile strain evolution was evaluated using DIC. Tensile loading was applied until failure with a universal tensile instrument (Instron 5500R) at a constant displacement rate of 0.02 mm/s. A raster speckle pattern was designed and printed with a dot size of 0.05 mm and a density of 75% to achieve a high-quality correlation [27,28]. DIC software (Vic-2D v6, Correlated Solutions, US) [29] was used to obtain the tensile deformation with a subset of 51 pixels and a step size of 5 pixels. Engineering strain was calculated from the displacement measurements, removing outliers with a 15-pixel Gaussian smoothing decay filter. The strain evolution in the sub-regions of the weldment was evaluated with virtual extensometers (nominated as Ext-1, 2 and 3), and the Ext-4 was wielded to measure the global strain evolution for laser-welded and PWHT samples (**Fig. 1**(b)).

2.4. Residual strain characterisation using PFIB-DIC

The PFIB-DIC ring-core method was used to quantify the residual strain at the fusion line (FZ/HAZ interface) and HAZ/BM interface. These regions usually contain dramatic microstructural changes and significant microscale residual strain which affects the peak position. Neutron diffraction is vulnerable to these microscale strains. Using the PFIB-DIC technique can validate that the residual lattice strain derived from neutron diffraction measurements is minimally affected by the insufficient microscale strain and can be representative to macroscale residual strain in loading direction. **Fig. 1**(c) shows the PFIB-DIC measurement position and how the incremental material removal was adopted to fabricate a ring-core with an inner diameter of 30 μm that contains enough grains to represent the macroscale residual strain given the pillar dimension is approximately three times the grain size [30]. The PFIB milling procedure was performed using a TESCAN MIRA 3 PFIB-SEM (University of Surrey, UK). When the milling depth reached the diameter of the ring-core, the residual strain is assumed to be fully released [31]. High-quality low-noise secondary electron images were obtained after each material removal step, with a spot size of 10 nm. A specifically developed automated program by TESCAN s.r.o. repeatedly conducted the incremental milling and image acquisition procedures. As reported elsewhere, MATLAB-based DIC software was used to visualise the strain relaxation using a resolution of 20 pixels and a subset size of 31 pixels for each increment [30,32].

2.5. Determination of stress-strain curve using spherical nanoindentation tip

The nanoindentation was conducted at the position (solid light blue dot in **Fig. 1**(d)) to determine the stress-strain curve for the sub-regions of the laser-welded sample. The load control was used to

conduct the indentation in a multicycle mode using a spherical diamond indenter with a ball radius of 4.25 μm from Ultra Indentation Tester (UNHT), CSM. The stepwise force were applied in 13 loading cycle until increasing to 100 mN with unloading of the half of maximum load of the cycle. A dwell time of 60s was used at the maximum load in each cycle to minimise the thermal drift. The load-displacement data were analysed with the Oliver and Pharr method [33] by fitting the unloading curve of each cycle to a power law to obtain contact stiffness, S, which was used to calculate the contact depth (h_c) and area (A). The spherical indentation tip was selected because of its advantages of enabling a continuous change of the mean pressure and characteristic strain as the indenter advances into the material [34]. A wide range of analytical formulations have been developed to calculate effective values of indentation stress and strain, which could depend on the instrument, materials, and test procedures. In previous studies [34], it's found that the geometrical definition of contact radius provides a better fit of elastic properties compared with the Hertz' contact mechanics. Therefore, in this work, the contact radius was then calculated using the indenter radius (R_i) standard geometric construction of a spherical cap ($a_c = \sqrt{2h_cR_i - {h_c}^2}$). The indentation strain and stress are defined by the widely used expression originally presented by Tabor, where the empirical factors are employed ($\varepsilon_{IT} = 0.2\frac{a_c}{R_i}$ and $\sigma_{IT} = \frac{L}{2.8A}$) [35].

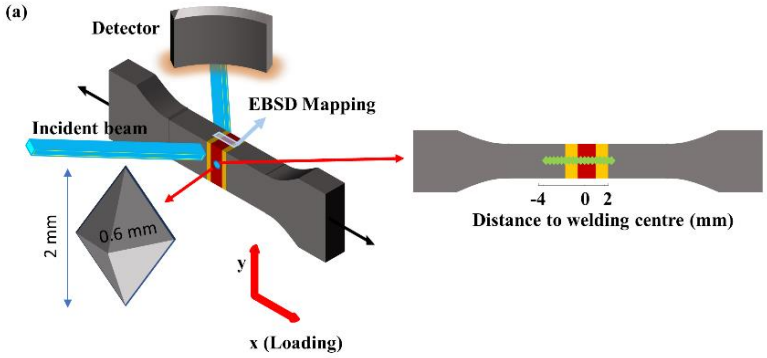
(a)
Detector
EBSD Mapping
Incident beam
2 mm
0.6 mm
y
x (Loading)
-4 0 2
Distance to welding centre (mm)

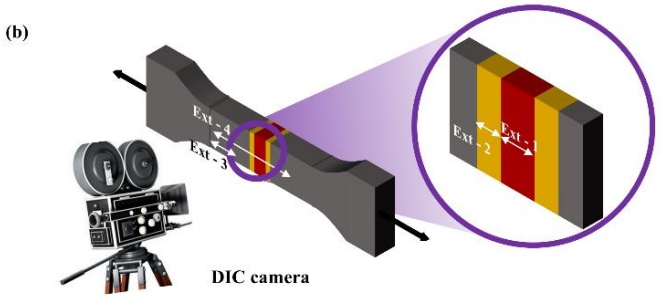
(b)
Ext - 4
Ext - 3
Ext - 2
Ext - 1
DIC camera

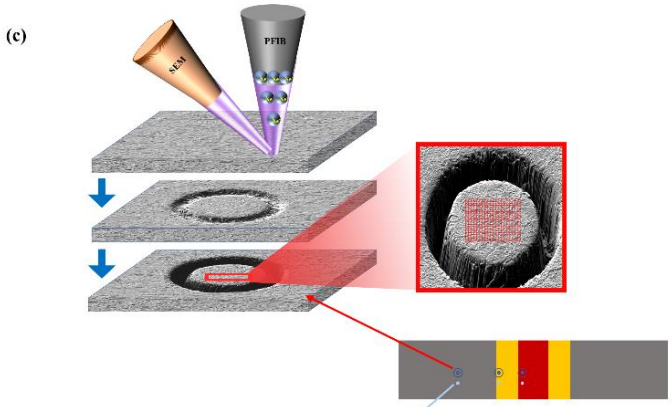
(c)
SEM
PFIB

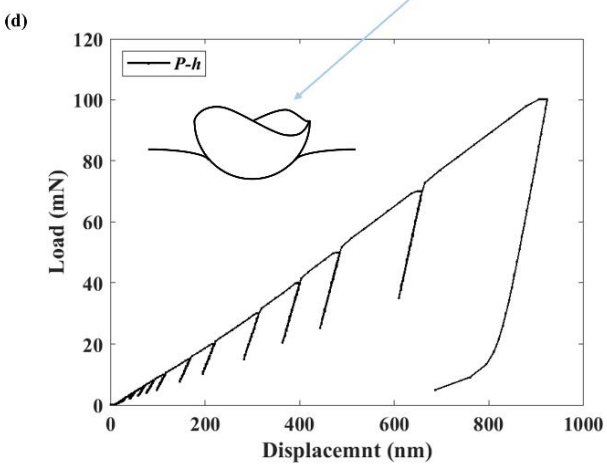
(d)
P-h
Load (mN)
Displacemnt (nm)
0
20
40
60
80
100
120
0
200
400
600
800
1000

Fig. 1 Schematic figures of the experimental setup. (a) *In situ* neutron diffraction lattice strain measurements and residual lattice strain measurements prior to loading. Inset figure shows the line scans were performed at 300 μm intervals, covering the three sub-regions during uniaxial tension. (b) Lab-based uniaxial tensile experiments were conducted, and strain evolution was analysed using Vic-2D DIC system. The virtual extensometers (Ext-1-4) are highlighted for macro strain measurements in different regions. (c) Incremental PFIB milling procedures during which residual strain is released. Sequence of secondar electron mages were acquired for residual strain analysis using MATLAB-based DIC method. (d) Nanoindentation experiments were performed using a spherical indenter with 13 cycles of load and unload procedures at the highlighted position in fusion line, HAZ/BM interface, and BM region.

3. Results

3.1. Microstructures

The stitched EBSD orientation maps in inverse pole figure (IPF) colouring, pole figures (PFs), and IPFs are shown in Fig. 2. Based on the microstructural characterisation of phases, grain size, and the nature of any precipitates, the weldment is conventionally divided into three sub-regions, i.e., FZ, HAZ, and BM regions. The selected single laser welding technique induced narrow FZ and HAZ regions with widths of ~1.2 mm and 1.4 mm, respectively. The average dimension of the grain size across the weldment in the loading direction varies, being 18.1 ± 1.1 μm in the FZ region and 10.7 ± 0.6 μm in the HAZ region. and 12.3 ± 0.7 μm in the BM region. The high thermal input leads to full austenitisation and grain growth in the FZ region, whilst partial austenitisation and subsequent martensitic phase transformations are evident in the HAZ region. The crystal dimension changes dramatically around the fusion line, although there is a narrow transition area. In the BM region, the grain size resembles the as-received materials. The PF indicates a weak imprecise texture for the measured (110) crystal plane, and the IPF implies isotropic properties in the loading direction in both the FZ and HAZ regions.

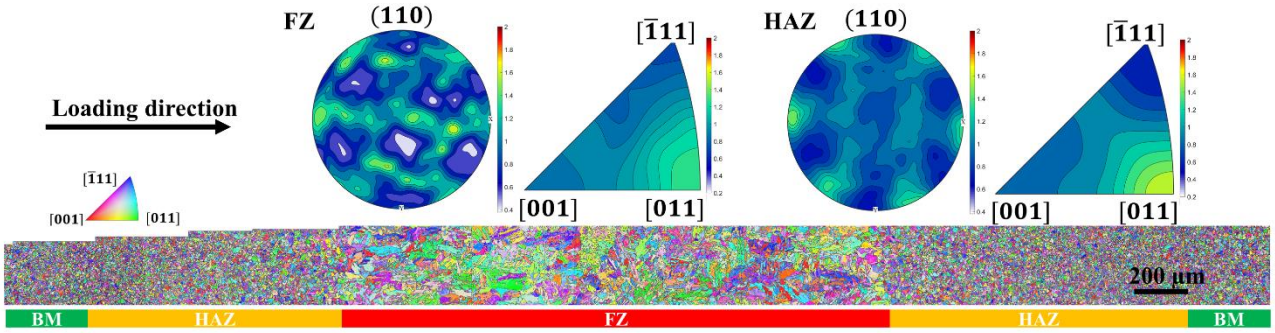

Fig. 2 EBSD orientation map in IPF colouring across the weldment. On the top of the EBSD orientation map is the PF of (110) crystal plane and IPF in the loading direction for the FZ and HAZ regions, respectively.

3.2. Macro-scale tensile strain evolution characterisation using DIC

The tensile strain evolution was measured using DIC technique while the laser-welded and PWHT samples were deformed. As shown in **Fig. 1**(c), the virtual extensometers were applied to quantify strain evolution in sub-regions of the weldment (Ext-1,2 and 3) and the global strain evolution of the whole gauge volume (Ext-4). The engineering stress–strain curves, before necking, are shown in **Fig. 3**(a) and **Fig. 3**(c). Yield stress was measured with a standard 0.2% offset on the stress-strain curves. The FZ region shows a higher yield strength of 539 MPa than the HAZ region (519 MPa). The global yield stress of the laser-welded sample (484 MPa) is higher than that of the PWHT sample (444 MPa). The inset figure in **Fig. 3**(a) shows that once the laser-welded sample commenced plastic deformation, the FZ and HAZ regions deformed less than the BM region. **Fig. 3**(b) visualises the accumulation of heterogeneous localised strain in the low-strength BM region at different applied loads during tensile deformation. The position where the local strain accumulates significantly indicates the possible fracture occurrence in the corresponding region. Closer inspection of the weld region in the early stages of deformation shows that the strain evolution around the fusion line is as significant as that in the BM region, whereas minor strain evolution is observed in the FZ centre and at the HAZ/BM interface. Looking at **Fig. 3**(d), only a small inhomogeneous tensile strain evolution was observed in the PWHT samples, and the highest strain evolution was observed around the HAZ/BM interface.

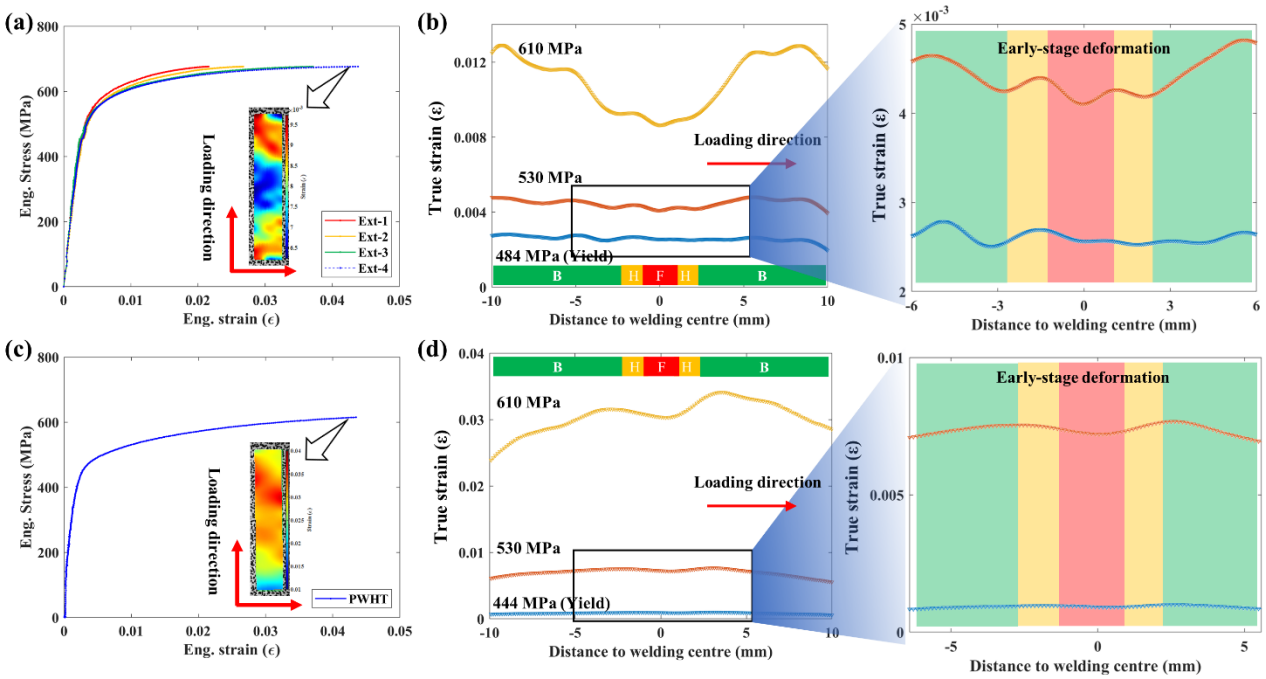

Fig. 3 Tensile performance of laser-welded and PWHT samples derived from the lab-based uniaxial tension. (a) & (c) Engineering stress–strain curves for the loading direction. The inset figure shows the 2D heterogeneous strain evolution maps across the sample. (b) & (d) Heterogeneous strain evolution occurs in sub-regions of the weldment at different applied stress. The colour bars in (b) and (d) show the sub-region of the weldment, where the F is FZ region, H is HAZ region and B is BM region

3.3. Micro-scale strain evolution characterisation using spherical indenter

Fig. 4(a) recorded the real-time load-displacement curves during the multiple cyclic loading and unloading. Compared to the fusion line and HAZ/BM interfaces, the deepest penetration was disclosed in the BM region at the same load. The scatter in **Fig. 4**(b-d) shows the indentation stress and strain derived by the equation introduced above. The curves present the representative plastic deformation behaviour which was expressed by fitting the scattering using a power law equation ($\sigma_{IT} = K\varepsilon_{IT}^{n}$) via the strength coefficient (K) and indentation work hardening coefficient (n). The representative elastic tensile behaviour was described in dash line (**Fig. 4**(b-d)) by employing the Young's modules obtained from nanoindentation test. The indentation stress at yield point at interfaces and BM region were obtained from the interception between elastic and plastic fitting curve, which are 1396 MPa, 1527 MPa and 622 MPa, respectively. The indentation yield stress is higher than that measured from tensile test, which is likely arisen from indentation size effects, as the radius of 4.25 μm only cover one or a couple of grain that is of the order of ~18 μm in FZ region and ~12 μm in HAZ and BM regions. In addition, the definition of indentation strain-stress parameters (i.e., the true indenter radius as a

function of depth) and the yield point under indenter could be oversimplified here. However, acquiring detailed elastic and plastic properties in different sub-regions is desirable to establish predictive tools for lifespan of the engineering joints. The high-resolution and high-precision provide this technique unique advantages in measuring the narrow sub-regions of the weldments, and new and more rigid methods are under development.

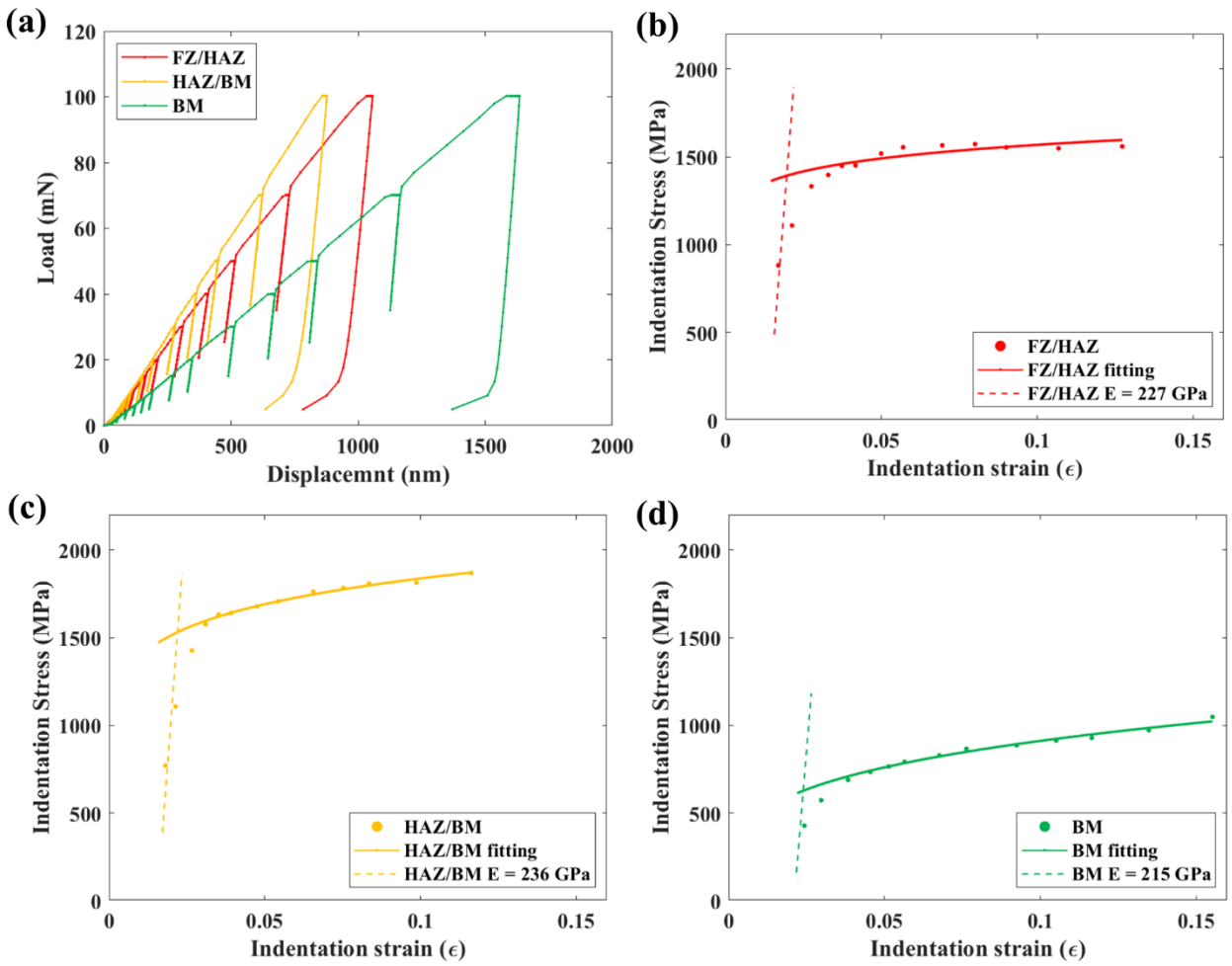

Fig. 4 Mechanical performance driven from sub-regions of laser-welded sample. (a) Load-displacement curves. (b-d) Scatter of indentation stress and strain, plastic behaviour curves fitted using power function and elastic behaviours described using Young's modules obtained from indentation test. The interception between the two curves indicates the indentation yield stress.

3.4. Lattice-scale strain evolution during uniaxial tension

To study the deformation of the laser-welded Eurofer97, *in situ* neutron diffraction measurement during tensile deformation was used to quantify the lattice strain evolution and investigate the interaction behaviour between residual strain and tensile deformation. The average measurement

uncertainty of the neutron diffraction was approximately $\pm 30\ \mu\varepsilon$ in the base material rising to approximately $\pm 70\ \mu\varepsilon$ in the FZ and HAZ [16]. As shown in **Fig. 5**(a), the lattice strain increases during tensile deformation, and a slightly lower lattice strain was observed in the FZ and HAZ regions at large deformation state (i.e. $\sigma = 610\ MPa$). A small degree of compressive lattice residual strain is induced in the <*110*>//LD grain family after unloading. To investigate the residual strain effect on tensile deformation, the global and local lattice strain evolution is extracted separately from the area highlighted by the rectangles in **Fig. 5**(a), and the lattice strain/applied stress curves in the four different regions are summarised in **Fig. 5**(b). In the elastic regime the lattice strain evolution is linear as a function of the engineering stress. Upon entering the plastic regime, it starts deviating from linearity. The HAZ/BM interface (Area-2) shows the highest yield strength (506 MPa) compared to the other areas (449 MPa), and a compressive shift in lattice strain is observed for the fusion line and HAZ/BM interface area. Comparing the slopes of the unloading curve, a similar stiffness is observed in all four areas.

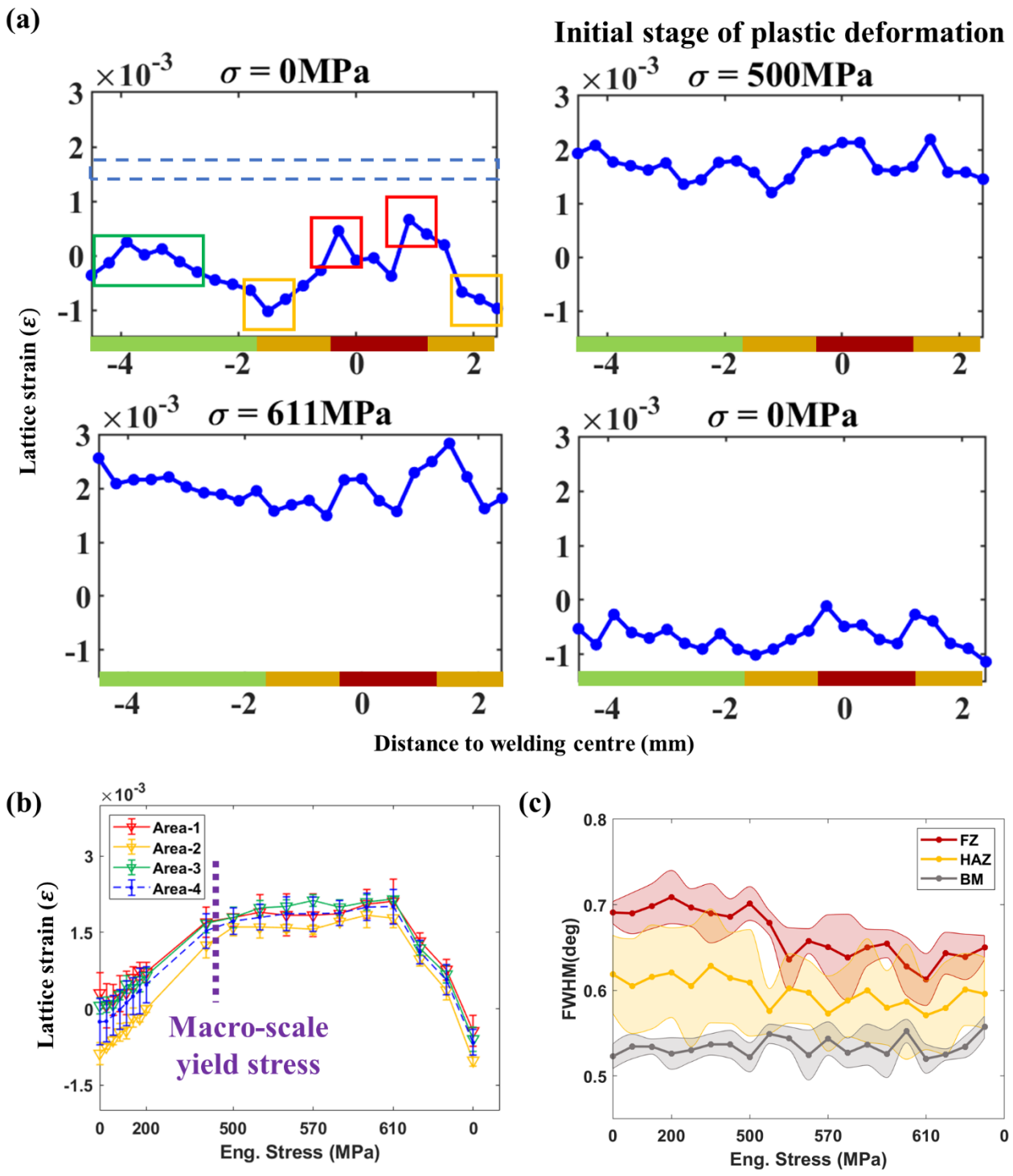

Fig. 5 Interaction between residual strain and applied strain for laser-welded sample. (a) Lattice strain distribution across the weldment at specific loads, e.g. initial residual strain state, initial plastic deformation, highest applied stress, and after unloading. The coloured bars indicate the sub-regions of the weldment. (b) Average lattice strain evolution at different regions is highlighted by the rectangles in (a), and the macro-scale yield stress is indicated. (c) FWHM evolution during the load and unload procedure.

The lattice strain evolution of PWHT sample during tensile deformation can be observed in **Fig. 6**(a). The full relief of the residual strain after PWHT in the loading direction is manifest, and the lattice strain distribution is homogeneous across the weldment under tension (**Fig. 6**(a)). A slightly lower applied strain was found in the welding region at the highest applied stress ($\sigma = 600\ MPa$), which indicate the microstructures were insufficiently restored. As was the case with the laser-welded sample, residual compressive strain is induced in the PWHT samples after unloading. The global lattice strain evolution of the PWHT sample is plotted as a function of engineering stress (**Fig. 6**(b)), indicating the linearity until 449 MPa. Although the tensile strength is similar with the global lattice strain evolution of the laser-welded sample, the stiffness of the PWHT sample is lower. As shown in **Fig. 5**(c) and **Fig. 6**(c), in contrast to the constant FWHM during the tensile deformation (0.52°) in the BM regions, a mild decline of FWHM is observed in the FZ and HAZ regions in the plastic regime, which may indicate a lower dislocation density. After the PWHT, the FWHM is similar across the sample and remains the same as in the BM region.

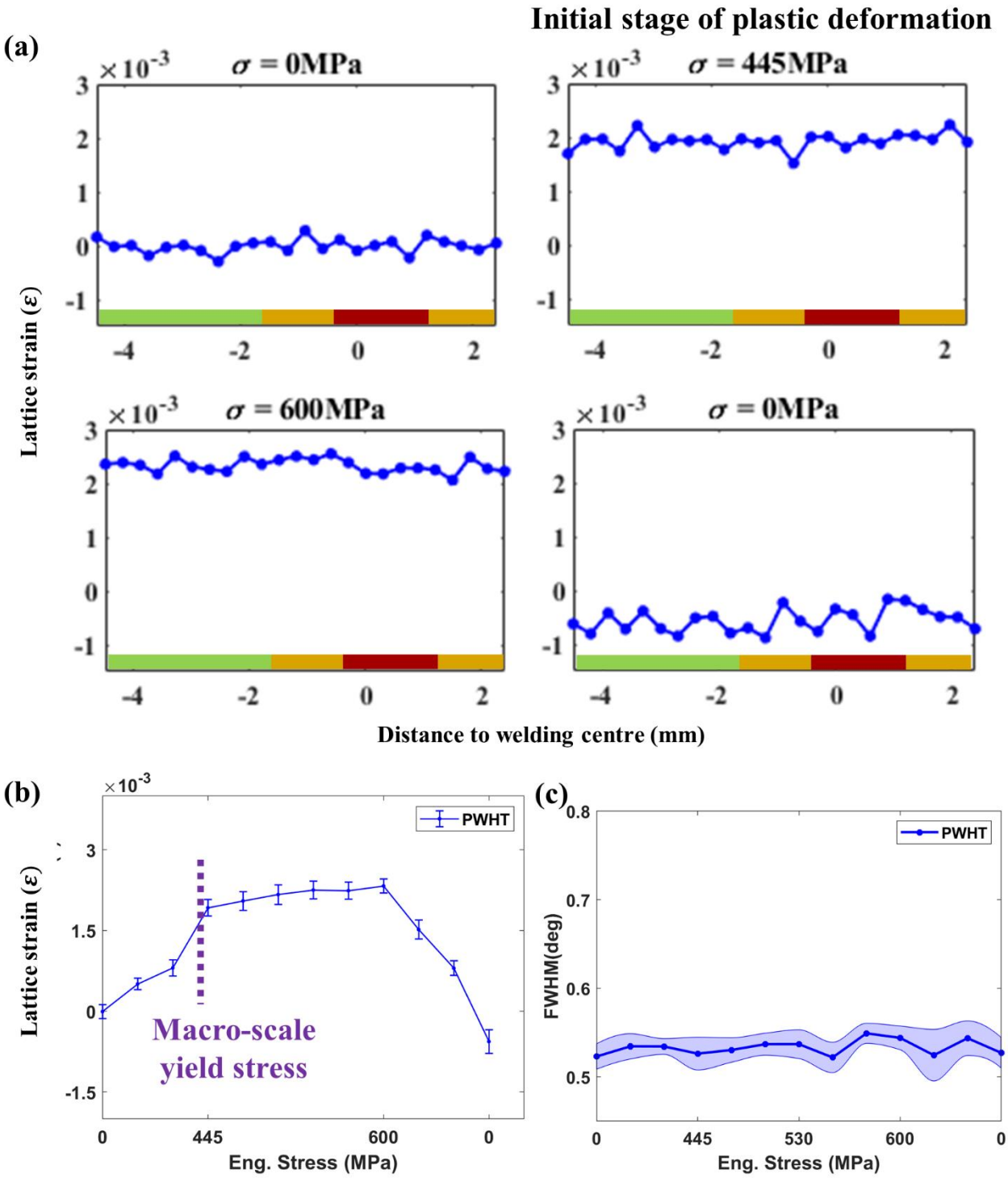

Fig. 6 Interaction between residual strain and applied strain for PWHT sample. (a), (b) & (c) are plotted in the same manner for the PWHT sample.

3.5. Residual strain characterisation in loading direction using neutron diffraction and PFIB-DIC

The residual strain distribution in the loading direction of laser-welded and PWHT Eurofer97 measured via neutron diffraction and the PFIB-DIC ring-core method is shown in **Fig. 7**. The residual lattice strain of <*110*>//LD grain families was characterised by neutron diffraction on laser-welded and PWHT samples. **Fig. 7**(a) shows a peak of residual tensile strain (with a magnitude of ~ $0.6 \times 10^{-3}\ \varepsilon$) in the FZ region, next to a trough of residual compressive strain (~$-1 \times 10^{-3}\ \varepsilon$) in the HAZ region. The PWHT reduces the residual strain substantially, as shown in **Fig. 7**(b). The measurement using neutron diffraction indicates that the residual strain is of a similar magnitude along the thickness direction. To overcome limitations of neutron diffraction in microscale strain, the PFIB-DIC ring-core method was employed to validate the results derived from neutron diffraction. The residual strain relaxation in the loading direction is characterised at the fusion line and at the HAZ/BM interface (**Fig. 7**(c)) using the PFIB-DIC method. Inversing the sign of the strain relaxation is the residual strain. The microscale strain is supposed to be maximum at measured positions due to the significant changes of microstructures and phase constituents. Additionally, the peak tensile/compressive residual strain is observed in these regions via neutron diffraction technique. The residual tensile strain derived using the PFIB-DIC technique is consistent with the results from neutron diffraction in the FZ region, although the residual compressive strain shows a slightly higher value (~$-1.6 \times 10^{-3}\ \varepsilon$) in the HAZ region, which validates reliability of using residual lattice strain of <*110*>//LD grain families to represent macroscale residual strain. Both techniques indicate there is almost negligible residual strain in BM region.

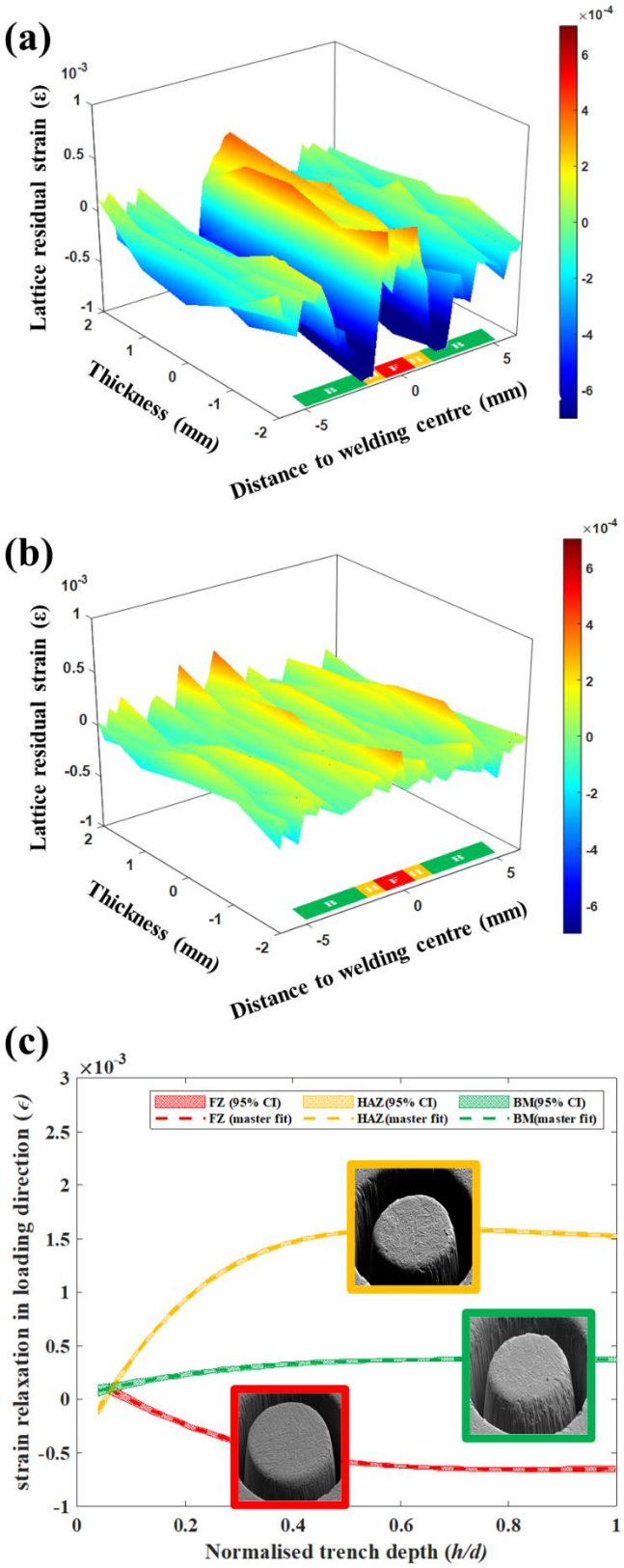

Fig. 7 (a) Residual strain distribution of <*110*>//LD grain family of laser-welded sample. (b) Residual strain distribution of <*110*>//LD grain family of PWHT sample. (c) Strain relaxation in loading direction measured

by the PFIB-DIC ring-core method at FZ line (red), HAZ/BM interface (yellow) and BM (green) region, respectively.

4. Discussion

In body centred cubic steels, the {110} family of planes are weakly affected by intergranular strains and can, therefore, be considered to represent the bulk mechanical properties of the material [36]. Here, the *<110>*//LD grain family is selected to study the residual strain and strain evolution with neutron diffraction. The residual strain distribution of laser-welded and PWHT Eurofer97 steel was investigated using neutron diffraction. As the narrow FZ and HAZ regions induced by the laser welding, a high-resolution measurement (0.6 mm) was applied to evaluate the residual strain distribution in the sub-regions. The 0.3 mm spacing between each gauge centre position results in 0.3 mm overlaps to achieve a high spatial resolution residual strain measurement in the loading direction. The FZ region shows residual tensile strain due to solidification shrinkage of the molten steel balanced by compressive strain in the HAZ regions [37]. The magnitude of residual strain is lower around the centre of the FZ region because of the offset of compressive strain from the martensitic phase transformation [38]. The measured residual lattice strain distribution trend is consistent with the neutron diffraction measurements on autogenous laser-welded Grade 91 steel [16,17,39,40]. The similar magnitude of residual strain distribution in the thickness direction indicates a full weld penetration and a symmetrical thermal history. As the neutron diffraction is affected by the microscale residual strain and deviation of composition, resulting in challenges in measuring the residual strain in the small sub-regions, validating the residual strain measurement is necessary. The PFIB-DIC ring-core method was applied to validate the residual strain in the loading direction to ensure the microscale strain in both laser-welded and PWHT Eurofer97 does not affect the neutron diffraction measurement. As the texture was weak in the loading direction (see inset IPF of **Fig. 2**), the micro-strain (inter/intra-granular residual strain) was in self-equilibrium. Therefore, the PFIB-DIC measurement evaluated the macro-scale residual strain [30], which can be directly compared with the neutron diffraction measurements. The consistency of residual strain between the two techniques confirms that the uncertainty of the neutron diffraction measurements caused by the application of the reference lattice spacing is in a reasonable range, validating the precision of the measurements arising from the neutron diffraction.

The global lattice strain curve of *<110>*//LD grain family began to yield at 449 MPa (Area-4 in **Fig. 5**(b) and **Fig. 6**(b)), which is slightly earlier than observed on the macro-scale. This is attributed to other grain families continuing to deform elastically. Those grain families also bears more load, which

results in a slight compressive shift of the <*110*>//LD grain family relative to the elastic regime [40]. Furthermore, it is reported that the stiffness of the grain families decreases in the order {222}, {110}, {321}, {211}, {310}, and {200} in Grade 91 steel (body centred cubic structure) [40]. Although the characterisation of other grain families has not been achieved, the non-linearity of lattice strain evolution in the plastic regime is consistent with the gradual stress transfer from stiffer crystal orientations to the more compliant ones [40–42]. The FWHM value of 0.52° in the BM region is consistent with previous studies of laser-welded Eurofer97 steel carried out using neutron diffraction [16]. The decrease of FWHM in the FZ and HAZ regions might be attributed to the elimination of free dislocations and lath boundaries (sub-grain boundaries) [43,44]. The FZ region contained more martensitic lath boundaries than the HAZ region, which might explain the large decrease in the FWHM value.

For a reliable lifetime assessment of welded components, knowledge of the tensile strain evolution is usually required to demonstrate the yield strength mismatch between sub-regions in weldments. The sub-region with the lowest strain evolution carries more load than the surrounding regions once the sample enters the plastic regime, leading to the elastic-plastic strain mismatch. This mismatch alters the intensity of local plastic deformation, consequently accelerating the initiation of cracks and affecting fracture toughness [45–47]. Using conventional mechanical tests, it is almost impossible to measure the strain evolution in such a small sub-region. Applying nanoindentation technique and combining uniaxial tension tests with the *in situ* neutron diffraction and lab-based DIC enables the high-resolution characterisation of the microscale, lattice-scale and macroscale strain evolution in the loading direction, respectively. The heterogeneous tensile properties of the laser-welded sample in **Fig. 3**(a) indicates localised strain is accumulated in the BM regions, implying that deformation occurs more extensively than in the remaining material through necking and on to fracture. Less deformation was observed in the FZ and HAZ regions (**Fig. 3**(b) and **Fig. 4**(b-d)) due to the presence of martensite, which enables more load to be carried than in the other regions in the plastic regime [21,48]. This is demonstrated with multi cycle indentation test, where FZ and HZA regions have higher yield strength than BM region, together with indicative stress-strain evolution. The increase in carbon in solution, owing to carbide dissolution in the FZ region, is another cause of strengthening [21,40]. The refined grains strengthen the material in the HAZ according to the Hall-Patch effect [49,50]. The microstructural strengthening gradually diminishes while moving to the BM region, where the microstructure is very similar to that of the parent material.

The heterogeneous strain distribution in the magnified part of **Fig. 3**(b) implies that the significant tensile deformation is driven by the residual tensile strain at the fusion line. By contrast, the residual compressive strain at the HAZ/BM interface hinders local tensile deformation. Similar conditions were

also found from the *<110>//LD* grain family (**Fig. 5**(a) and (b)) and microscale indentation stress-strain curves (**Fig. 4**(b-d)). The quantitative strain evaluation characterisation via *in situ* neutron diffraction indicates an increase in yield strength to 506 MPa at the HAZ/BM interface (Area-2). Conversely, the residual tensile strain degraded the yield strength at the fusion line (Area-1) to the same as that in the BM region. Additionally, the residual strain effect is substantial during the elastic deformation and initial stage of plastic deformation (magnified figures in **Fig. 3**(b) and **Fig. 3**(d)). The increasing plastic deformation, however, limits the residual strain effect in the total strain evaluation because the induced tensile deformation changes the residual strain states. This implies that the microstructure dominated local strengthening in the FZ and HAZ regions at large plastic deformation. A small degree of compressive lattice residual strain was found in the *<110>*//LD grain family after unloading for both laser-welded and PWHT samples, which might be attributed to the reverse plastic flow on unloading [7]. A comparison with a previous evaluation of tensile strain evolution carried out on Grade 91 steel joint [22] shows that the present results display a comprehensive underpinning understanding of the deformation mechanism due to the establishment of the correlation between residual strain, microstructure, and tensile properties in the sub-regions of the weldment.

The PWHT lowered the global yield strength to around 444 MPa by inducing tempering of martensite and formation of fine precipitates, which is consistent with previous investigations [21,22]. The FWHM dropped in the FZ and HAZ regions, indicating that the tensile strength degraded due to a decrease in the dislocation density [51]. Although the microstructure was not fully restored and a slightly heterogeneous strain evolution **(Fig. 3**(d) and **Fig. 6**(a)) was found in the weld region when high plastic deformation was applied, the PWHT eliminated residual strain in the loading direction entirely and reduced the strain mismatch around the fusion line and at the HAZ/BM interface significantly. In addition, without the prevention of residual compressive residual strain, the strain accumulation and fracture tended to occur at the HAZ/BM interface as a result of the residual mismatch between the two microstructures.

5. Conclusions

The residual strain distribution in the loading direction has been obtained using neutron diffraction and the PFIB-DIC ring-core method. The tensile strain evolution in a laser-welded and PWHT Eurofer97 steel during tensile deformation has been measured using *in situ* Neutron diffraction and lab-based tensile-DIC. The principal conclusions of this study are:

1. The residual strain of laser-welded sample measured by neutron diffraction established that the highest residual tensile and compressive strain in the loading direction is found around the fusion line ($0.6 \times 10^{-3}\mu\varepsilon$) and at the HAZ/BM interface ($-1 \times 10^{-3}\mu\varepsilon$). The three PFIB-DIC ring-core measurements from around the fusion line, the HAZ/BM interface, and the BM region confirmed the findings of the neutron diffraction.
2. The *in situ* neutron diffraction and lab-based tensile-DIC strain evaluation showed that the FZ and HAZ region of laser-welded sample withstand more load once the applied stress exceeds the yield point of the material because of the microstructural strengthening. The residual compressive strain then induced the superimposed strengthening effect on the local tensile strength to 506 MPa near the HAZ/BM interface, which was distinctly higher than in the surroundings. Such mismatch accelerates crack initiation and affects the fracture toughness.
3. The selective PWHT is effective in mitigation of residual strain and elimination of elastic-plastic mismatch between sub-regions of the weldment.
4. The residual strain affects the tensile behaviour significantly at the initial deformation stage, and the microstructural strengthening mechanism dominates in the later stages of deformation.

6. Acknowledgements

The authors give thanks to the Karlsruhe Institute of Technology for providing the Eurofer97 plate for this study and Dr Simon Kirk (UKAEA) for his advice on laser welding. The authors thank the Institut Laue-Langevin (ILL) for providing the beamtime at SALSA (DOI: 10.5291/ILL-DATA.1-02-342). The authors would also like to thank Dr Sandra Cabeza and Sergio Martinez Garcia, from ILL, and Mr David Jones, from the University of Surrey, for their support and assistance during the sample preparation, experiment, and data analysis. This work has been carried out within the framework of the EUROfusion Consortium and has received (part) funding from the Euratom Research and Training Programme 2014 - 2018 and 2019 - 2020 under grant No. 633053. The views and opinions expressed herein do not necessarily reflect those of the European Commission. Dr Sui, Dr Zhu, Dr Wang and Dr Gorley would also like to acknowledge the EPSRC grants (EP/W006839/1) and the UK Government Department for Business, Energy and Industrial Strategy for their time and resources. Dr Sui would like to acknowledge funding from the Royal Academy of Engineering under the Industrial Fellowships programme. Dr Zhang would like to thank the National Measurement System Programme of the UK Government Department for Business, Energy and Industrial Strategy for financial support. Part of

this work was supported by grants from the EPSRC project (EP/P001521/1) “Integrated Plasma Source Focused Ion Beam with Scanning Electron Microscope.”

7. Author contribution

Bin Zhu: Methodology, Investigation, Formal analysis, Writing – original draft, Writing – review & editing.

Nathanael Leung: Investigation, Writing – review & editing.

Yiqiang Wang: Supervision, Funding, Conceptualisation, Methodology, Writing – review & editing.

Hannah, Zhang: Investigation, Writing – review & editing.

Jiří Dluhoš: Methodology, Writing – review & editing.

Thilo Pirling: Investigation, Writing – review & editing.

Michael Gorley: Supervision, Writing – review & editing.

Mark J. Whiting: Supervision, Writing – review & editing.

Tan Sui: Supervision, Funding, Conceptualisation, Methodology, Writing – review & editing.

8. Reference

[1] Poitevin Y, Aubert Ph, Diegele E, de Dinechin G, Rey J, Rieth M, et al. Development of welding technologies for the manufacturing of European Tritium Breeder blanket modules. Journal of Nuclear Materials 2011;417:36–42. https://doi.org/10.1016/J.JNUCMAT.2010.12.259.

[2] Jones LP, Aubert P, Avilov V, Coste F, Daenner W, Jokinen T, et al. Towards advanced welding methods for the ITER vacuum vessel sectors. Fusion Engineering and Design 2003;69:215–20. https://doi.org/10.1016/S0920-3796(03)00341-7.

[3] Kirk S, Suder W, Keogh K, Tremethick T, Loving A. Laser welding of fusion relevant steels for the European DEMO. Fusion Engineering and Design 2018. https://doi.org/10.1016/j.fusengdes.2018.03.039.

[4] Wu S, Zhang J, Yang J, Lu J, Liao H, Wang X. Investigation on microstructure and properties of narrow-gap laser welding on reduced activation ferritic/martensitic steel CLF-1 with a thickness of 35 mm. Journal of Nuclear Materials 2018;503:66–74. https://doi.org/10.1016/j.jnucmat.2018.02.038.

[5] Aubert P, Tavassoli F, Rieth M, Diegele E, Poitevin Y. Low activation steels welding with PWHT and coating for ITER test blanket modules and DEMO. Journal of Nuclear Materials 2011;409:156–62. https://doi.org/10.1016/J.JNUCMAT.2010.09.009.

[6] Aubert P, Tavassoli F, Rieth M, Diegele E, Poitevin Y. Review of candidate welding processes of RAFM steels for ITER test blanket modules and DEMO. Journal of Nuclear Materials 2011;417:43–50. https://doi.org/10.1016/J.JNUCMAT.2010.12.248.

[7] Withers PJ. Residual stress and its role in failure. Reports on Progress in Physics 2007;70:2211–64. https://doi.org/10.1088/0034-4885/70/12/R04.

[8] Donné AJ. Roadmap Towards Fusion Electricity (Editorial). Journal of Fusion Energy 2019;38. https://doi.org/10.1007/s10894-019-00223-7.

[9] Fernández P, Lancha AM, Lapeña J, Serrano M, Hernández-Mayoral M. Metallurgical properties of reduced activation martensitic steel Eurofer'97 in the as-received condition and after thermal ageing. Journal of Nuclear Materials 2002;307–311:495–9. https://doi.org/10.1016/S0022-3115(02)01013-9.

[10] Zeman A, Debarberis L, Kočík J, Slugeň V, Keilová E. Microstructural analysis of candidate steels pre-selected for new advanced reactor systems. Journal of Nuclear Materials 2007;362:259–67. https://doi.org/10.1016/j.jnucmat.2007.01.068.

[11] Li XX, Li XX, Schönecker S, Li R, Zhao J, Vitos L. Understanding the mechanical properties of reduced activation steels. vol. 146. Elsevier Ltd; 2018. https://doi.org/10.1016/j.matdes.2018.03.009.

[12] Andreani R, Diegele E, Laesser R, Van Der Schaaf B. The European integrated materials and technology programme in fusion. Journal of Nuclear Materials, vol. 329–333, North-Holland; 2004, p. 20–30. https://doi.org/10.1016/j.jnucmat.2004.04.339.

[13] Lässer R, Baluc N, Boutard JL, Diegele E, Dudarev S, Gasparotto M, et al. Structural materials for DEMO: The EU development, strategy, testing and modelling. Fusion Engineering and Design 2007;82:511–20. https://doi.org/10.1016/j.fusengdes.2007.06.031.

[14] Richardson M, Gorley M, Wang Y, Aiello G, Pintsuk G, Gaganidze E, et al. Technology readiness assessment of materials for DEMO in-vessel applications. Journal of Nuclear Materials 2021;550:152906. https://doi.org/10.1016/j.jnucmat.2021.152906.

[15] Tanigawa H, Maruyama T, Noguchi Y, Takeda N, Kakudate S. Laser welding to expand the allowable gap in bore welding for ITER blanket hydraulic connection. Fusion Engineering and Design 2015;98–99:1634–7. https://doi.org/10.1016/j.fusengdes.2015.06.155.

[16] Hughes DJ, Koukovini-Platia E, Heeley EL. Residual stress in a laser welded EUROFER blanket module assembly using non-destructive neutron diffraction techniques. Fusion Engineering and Design 2014;89:104–8. https://doi.org/10.1016/j.fusengdes.2013.12.041.

[17] Kumar S, Kundu A, Venkata KA, Evans A, Truman CE, Francis JA, et al. Residual stresses in laser welded ASTM A387 Grade 91 steel plates. Materials Science and Engineering A 2013;575:160–8. https://doi.org/10.1016/j.msea.2013.03.046.

[18] Lu G, Sokol DW, Zhang Y, Dulaney JL. Nanosecond pulsed laser-generated stress effect inducing macro-micro-nano structures and surface topography evolution. Appl Mater Today 2019;15. https://doi.org/10.1016/j.apmt.2019.01.005.

[19] Coppola R, Asserin O, Aubert P, Braham C, Monnier A, Valli M, et al. Characterisation of residual stresses in Eurofer welded specimens: Measurements by neutron diffraction and comparison with weld modeling. Journal of Nuclear Materials 2011;417:51–4. https://doi.org/10.1016/j.jnucmat.2010.12.051.

[20] Zhu B, Wang Y, Dluhoš J, London AJ, Gorley M, Whiting MJ, et al. A novel pathway for multiscale high-resolution time-resolved residual stress evaluation of laser-welded Eurofer97. Sci Adv 2022;8. https://doi.org/10.1126/sciadv.abl4592.

[21] Zhu B, Leung N, Kockelmann W, Kabra S, London AJ, Gorley M, et al. Revealing the residual stress distribution in laser welded Eurofer97 steel by neutron diffraction and Bragg edge imaging. J Mater Sci Technol 2022;114:249–60. https://doi.org/https://doi.org/10.1016/j.jmst.2021.12.004.

[22] Harte A, Dawson H, Bowden D, Spencer R, Kirk S, Gorley M. Deformation heterogeneity in laser-welded Eurofer. Fusion Engineering and Design 2020;161:111860. https://doi.org/10.1016/j.fusengdes.2020.111860.

[23] Rieth M, Schirra M, Falkenstein A, Graf P, Heger S, Kempe H, et al. EUROFER 97 Tensile, charpy, creep and structural tests. Germany: 2003.

[24] Mainprice D, Hielscher R, Schaeben H. Calculating anisotropic physical properties from texture data using the MTEX open-source package. Geol Soc Spec Publ 2011;360:175–92. https://doi.org/10.1144/SP360.10.

[25] Roebuck B, Bennett EG, Dickson A. The measurement of uncertainty in grain size distribution. Interlaboratory exercise part 1-reference images. National Physical Lab.; 1999.

[26] Pirling T, Bruno G, Withers PJ. SALSA-A new instrument for strain imaging in engineering materials and components. Materials Science and Engineering A 2006;437. https://doi.org/10.1016/j.msea.2006.04.083.

[27] Schreier H, Orteu JJ, Sutton MA. Image correlation for shape, motion and deformation measurements: Basic concepts, theory and applications. 2009. https://doi.org/10.1007/978-0-387-78747-3.

[28] Dong YL, Pan B. A Review of Speckle Pattern Fabrication and Assessment for Digital Image Correlation. Exp Mech 2017;57. https://doi.org/10.1007/s11340-017-0283-1.

[29] Student REU, Cintr R, Mentor REU, Saouma V, Rico P, Summer B. Strain Measurements with the Digital Image Correlation System Vic-2D. Image (Rochester, NY) 2008.

[30] bin Zhu, Yiqiang Wang, Jiří Dluhoš, London J. Andy, Michael Gorley, Whiting J. Mark, et al. A novel pathway for multiscale high-resolution time-resolved residual stress evaluation of laser-welded Eurofer97. Sci Adv 2022;8:eabl4592. https://doi.org/10.1126/sciadv.abl4592.

[31] Sui T, Lunt AJG, Baimpas N, Sandholzer MA, Li T, Zeng K, et al. Understanding nature's residual strain engineering at the human dentine-enamel junction interface. Acta Biomater 2016;32. https://doi.org/10.1016/j.actbio.2016.01.009.

[32] Digital Image Correlation and Tracking - File Exchange - MATLAB Central n.d. https://uk.mathworks.com/matlabcentral/fileexchange/50994-digital-image-correlation-and-tracking (accessed June 18, 2020).

[33] Pharr GM. An improved technique for determining hardness and elastic modulus using load and displacement sensing indentation experiments. J Mater Res 1992;7:1564–83. https://doi.org/10.1557/JMR.1992.1564.

[34] Ruiz-Moreno A, Hähner P, Fumagalli F, Haiblikova V, Conte M, Randall N. Stress−strain curves and derived mechanical parameters of P91 steel from spherical nanoindentation at a range of temperatures. Mater Des 2020;194:108950. https://doi.org/10.1016/j.matdes.2020.108950.

[35] Tabor D. The hardness of metals. Oxford university press; 2000.

[36] Biswal R, Mehmanparast A, Ganguly S, Kelleher J. Experimental Investigation of Lattice Deformation Behavior in S355 Steel Weldments Using Neutron Diffraction Technique. J Mater Eng Perform 2021;30. https://doi.org/10.1007/s11665-021-06104-5.

[37] Lai H-HH, Wu W. Practical examination of the welding residual stress in view of low-carbon steel welds. Journal of Materials Research and Technology 2020.

[38] Rossini NS, Dassisti M, Benyounis KY, Olabi AG. Methods of measuring residual stresses in components. Mater Des 2012;35:572–88. https://doi.org/10.1016/J.MATDES.2011.08.022.

[39] Suder W, Ganguly S, Williams S, Paradowska AM, Colegrove P. Comparison of joining efficiency and residual stresses in laser and laser hybrid welding. Science and Technology of Welding and Joining 2011;16:244–8. https://doi.org/10.1179/1362171810Y.0000000020.

[40] Shrestha T, Charit I, Potirniche G. In Situ Tensile Deformation and Residual Stress Measurement by Neutron Diffraction in Modified 9Cr-1Mo Steel. J Mater Eng Perform 2015;24:4710–20. https://doi.org/10.1007/s11665-015-1752-2.

[41] Tang L, Wang L, Wang M, Liu H, Kabra S, Chiu Y, et al. Synergistic deformation pathways in a TWIP steel at cryogenic temperatures: In situ neutron diffraction. Acta Mater 2020;200. https://doi.org/10.1016/j.actamat.2020.09.075.

[42] Weisser MA, Evans AD, van Petegem S, Holdsworth SR, van Swygenhoven H. In situ room temperature tensile deformation of a 1% CrMoV bainitic steel using synchrotron and neutron diffraction. Acta Mater 2011;59:4448–57. https://doi.org/10.1016/j.actamat.2011.03.068.

[43] Wang L, Li M, Almer J. Investigation of deformation and microstructural evolution in Grade 91 ferritic–martensitic steel by in situ high-energy X-rays. Acta Mater 2014;62:239–49. https://doi.org/10.1016/j.actamat.2013.10.003.

[44] Giroux PF, Dalle F, Sauzay M, Malaplate J, Fournier B, Gourgues-Lorenzon AF. Mechanical and microstructural stability of P92 steel under uniaxial tension at high temperature. Materials Science and Engineering A 2010;527. https://doi.org/10.1016/j.msea.2010.03.001.

[45] Coules HE, Horne GCM, Abburi Venkata K, Pirling T. The effects of residual stress on elastic-plastic fracture propagation and stability. Mater Des 2018;143:131–40. https://doi.org/10.1016/j.matdes.2018.01.064.

[46] Qian X, Dodds RH, Choo YS. Elastic-plastic crack driving force for tubular K-joints with mismatched welds. Eng Struct 2007;29. https://doi.org/10.1016/j.engstruct.2006.06.024.

[47] Noroozi AH, Glinka G, Lambert S. Prediction of fatigue crack growth under constant amplitude loading and a single overload based on elasto-plastic crack tip stresses and strains. Eng Fract Mech 2008;75. https://doi.org/10.1016/j.engfracmech.2007.03.024.

[48] Oliver EC, Daymond MR, Withers PJ. Interphase and intergranular stress generation in carbon steels. Acta Mater 2004;52. https://doi.org/10.1016/j.actamat.2003.12.035.

[49] Hall EO. The Deformation and Ageing of Mild Steel: III Discussion of Results. Proceedings of the Physical Society Section B 1951;64:747. https://doi.org/10.1088/0370-1301/64/9/303.

[50] Petch NJ. The cleavage strength of polycrystals. Journal of the Iron and Steel Institute 1953;174:25–8.

[51] Wang Y, Liu B, Yan K, Wang M, Kabra S, Chiu YL, et al. Probing deformation mechanisms of a FeCoCrNi high-entropy alloy at 293 and 77 K using in situ neutron diffraction. Acta Mater 2018;154:79–89. https://doi.org/10.1016/j.actamat.2018.05.013.